

Docetaxel Loaded Fluorescent Liquid Crystalline Nanoparticles for Cancer Theranostics

Valeria Meli, Claudia Caltagirone, Angela Maria Falchi, Stephen T Hyde, Vito Lippolis, Maura Monduzzi, Marc Obiols-Rabasa, Antonella Rosa, Judith Schmidt, Yeshayahu Talmon, and Sergio Murgia

Langmuir, **Just Accepted Manuscript** • DOI: 10.1021/acs.langmuir.5b02101 • Publication Date (Web): 20 Aug 2015

Downloaded from <http://pubs.acs.org> on August 25, 2015

Just Accepted

“Just Accepted” manuscripts have been peer-reviewed and accepted for publication. They are posted online prior to technical editing, formatting for publication and author proofing. The American Chemical Society provides “Just Accepted” as a free service to the research community to expedite the dissemination of scientific material as soon as possible after acceptance. “Just Accepted” manuscripts appear in full in PDF format accompanied by an HTML abstract. “Just Accepted” manuscripts have been fully peer reviewed, but should not be considered the official version of record. They are accessible to all readers and citable by the Digital Object Identifier (DOI®). “Just Accepted” is an optional service offered to authors. Therefore, the “Just Accepted” Web site may not include all articles that will be published in the journal. After a manuscript is technically edited and formatted, it will be removed from the “Just Accepted” Web site and published as an ASAP article. Note that technical editing may introduce minor changes to the manuscript text and/or graphics which could affect content, and all legal disclaimers and ethical guidelines that apply to the journal pertain. ACS cannot be held responsible for errors or consequences arising from the use of information contained in these “Just Accepted” manuscripts.



1
2
3
4
5
6
7
8
9
10
11
12
13
14
15
16
17
18
19
20
21
22
23
24
25
26
27
28
29
30
31
32
33
34
35
36
37
38
39
40
41
42
43
44
45
46
47
48
49
50
51
52
53
54
55
56
57
58
59
60

1 **Docetaxel Loaded Fluorescent Liquid Crystalline Nanoparticles for**
2
3
4
5
6 **Cancer Theranostics**

3 *Valeria Meli,^a Claudia Caltagirone,^{a*} Angela M. Falchi,^b Stephen T. Hyde,^c Vito Lippolis,^a Maura*
4 *Monduzzi,^a Marc Obiols-Rabasa,^d Antonella Rosa,^b Judith Schmidt,^e Yeshayahu Talmon,^e and*
5 *Sergio Murgia,^{a*}*

6
7 ^a Dipartimento di Scienze Chimiche e Geologiche, Università degli Studi di Cagliari, S.S. 554
8 Bivio per Sestu, 09042, Monserrato CA, Italy. E-mail: murgias@unica.it and
9 ccaltagirone@unica.it, Tel. +39(0)70 675 4453.

10 ^b Dipartimento di Scienze Biomediche, Università di Cagliari, s.s. 554 bivio Sestu, I-09042
11 Monserrato (CA), Italy.

12 ^c Department of Applied Mathematics, Research School of Physics and Engineering, The Australian
13 National University, Canberra, A.C.T. 0200, Australia.

14 ^d Division of Physical Chemistry, Department of Chemistry, Getingevägen 60, SE-22240
15 Lund, Sweden.

16 ^e Department of Chemical Engineering, Technion – Israel Institute of Technology, Haifa
17 3200003, Israel.

1
2
3 19 **Abstract**
4

5 20 Here, we describe a novel monoolein-based cubosome formulation engineered for possible
6
7 21 theranostic applications in oncology. The Docetaxel loaded nanoparticles were stabilized in water
8
9 22 by a mixture of commercial Pluronic (polyethylene oxide-polypropylene oxide-polyethylene oxide
10
11 23 triblock copolymer) F108 (PF108), and rhodamine- and folate-conjugated PF108, so that the
12
13 24 nanoparticles possess targeting, therapeutic, and imaging properties. Nanoparticles were
14
15 25 investigated by DLS, cryo-TEM, and SAXS to confirm their structural features. The fluorescent
16
17 26 emission characterization of the proposed formulation indicated that the rhodamine conjugated to the
18
19 27 PF108 experiences an environment less polar than water (similar to chloroform), suggesting that the
20
21 28 fluorescent fragment is buried within the polyethylenoxide corona surrounding the nanoparticle.
22
23 29 Furthermore, these nanoparticles were successfully used to image living HeLa cells and demonstrated a
24
25 30 significant short-term (4 h incubation) cytotoxicity effect against these cancer cells. Furthermore,
26
27 31 given their analogy as nanocarriers for molecules of pharmaceutical interest, and to better stress the
28
29 32 singularities of these bicontinuous cubic nanoparticles, we also quantitatively evaluated the
30
31 33 differences between cubosomes and multi-lamellar liposomes in terms of surface area and
32
33 34 hydrophobic volume.
34
35
36
37
38
39
40
41
42
43
44
45
46
47
48
49
50
51
52
53
54
55
56
57
58
59
60

1. Introduction

The amphiphilic characteristics of polar lipids drive their self-assembly in water, giving a number of liquid crystalline phases.^{1,2} Among them, the most interesting are probably the reverse bicontinuous cubic phases.³ These are a family of three-dimensional cubic structures constituted by a curved, non-intersecting lipid bilayer folded to form two disconnected, continuous water channels with a crystal lattice that can be described by three different types of infinite periodic minimal surfaces: the double diamond (space group $Pn\bar{3}m$), the gyroid (space group $Ia\bar{3}d$), and the primitive (space group $Im\bar{3}m$). These phases have been extensively investigated in recent decades because they represent versatile nanostructures able to incorporate molecules of biological relevance.⁴⁻⁸ Interestingly, cubic phases can be formulated as aqueous nanoparticle dispersions, known as cubosomes.⁹ Although various emulsifiers have been suggested,^{10,11} in general, the stabilization in water of such liquid crystalline nanoparticles is achieved using amphiphilic polymers having long polyethylene oxide (PEO) chains, e.g. Pluronics (polyethylene oxide-polypropylene oxide-polyethylene oxide triblock copolymers) or polysorbate 80.^{9,12} Similarly to the reverse liquid crystalline cubic bulk phases, pharmaceutical applications are predicted for cubosomes,¹³⁻¹⁷ and their potential use as nanocarriers for MRI probes has been investigated.^{18,19} These nanoparticles have also been proposed for theranostic applications.²⁰⁻²⁵ Indeed, several peculiar characteristics make cubosomes appealing as theranostic tools in oncology. Among these, one of the most distinguishing is the higher hydrophobic volume with respect to liposomes, often considered as the golden standard for lipid-based nanocarriers in medicine. However, a quantitative comparison of the hydrophobic portion of these two kinds of nanoparticles has never been reported in the literature. Other cubosomes specific features are the possibility of simultaneously host therapeutics and imaging agents, as well as a size (typically in the range 100-200 nm) that, at least in principle, allows the exploitation of the enhanced permeation retention mechanism for the passive targeting to cancer tissues.^{9,26} In view of their application as nanomedicine, it is also worth mentioning that the clearance from the bloodstream via the

1
2
3 61 mononuclear phagocytic system should be retarded since, in analogy with stealth liposomes, these
4
5 62 nanoparticles are enclosed within a sort of a PEO corona that should prevent efficient recognition
6
7 63 by opsonin, thus hindering phagocytosis.²⁷ Moreover, it was demonstrated that cubosomes (and
8
9 64 hexosomes) can be suitably formulated covering their surface with folate residues^{20,28} or anti-EGFR
10
11 65 Fab²⁹ to actively target these nanocarriers toward cancer cells, while the effects at subcellular level
12
13 66 of pristine monoolein-based cubosomes were recently investigated on HeLa cells.³⁰ Remarkably,
14
15 67 nanoparticles with reverse bicontinuous cubic internal structure endowed of long time stability and
16
17 68 thermoresponsive capabilities can be formulated using polymer-surfactant mixtures.³¹
18
19
20 69 To explore further the potential of lipid-based liquid crystalline nanoparticles as theranostic
21
22 70 nanomedicine in cancer treatments, we report here the loading of monoolein-based cubosomes with
23
24 71 a potent anticancer drug (Docetaxel). Such formulation was stabilized with a mixture of commercial
25
26 72 Pluronic F108 (PF108), folate-conjugated PF108 (PF108-FA), and rhodamine-conjugated PF108
27
28 73 (PF108-R) to simultaneously confer targeting, therapeutic, and imaging abilities on these
29
30 74 nanoparticles. It deserves noticing that engineering stable, multifunctional cubosome formulations
31
32 75 can be a hard task. While the hydrophobic effect represents the main force that drives the self-
33
34 76 assembly of the lipids constituting the nanoparticles, their inner phase is basically determined by the
35
36 77 geometrical features of the lipid hydrophobic tail and polar head. This is rationalized by the
37
38 78 molecular effective packing parameter (P_{eff}), given by the ratio v/al , where v and l are, respectively,
39
40 79 the hydrophobic chain volume and length (taken as 80% of the fully extended chain), and a is the
41
42 80 head group area.¹ P_{eff} is strongly dependent by the surrounding environment, therefore the type of
43
44 81 phase that characterizes the nanoparticles (and their very existence) is barely predictable in the
45
46 82 presence of additives, since encapsulation within the lipid bilayer of molecules useful to give these
47
48 83 nanoparticles theranostic skills may significantly alter P_{eff} , thus provoking the transition of the inner
49
50 84 phase or the collapse of the formulation.⁹ In addition, decoration of the cubosome surface with
51
52 85 targeting and/or fluorescent moieties may disturb both the colloidal stability of the formulation and
53
54 86 the cellular uptake of the nanoparticles. Throughout this paper we will demonstrate that the
55
56
57
58
59
60

1
2
3 87 proposed cubosome formulation, although prepared with a high portion (40%) of conjugated PF108
4
5 88 is stable, and successfully delivers its cargo to HeLa cells, taken as standard for cancer cells.
6
7 89 Moreover, considering the analogies between liposomes and cubosomes, we also presented here a
8
9 90 theoretical evaluation of the hydrophobic volume of these liquid crystalline nanoparticles.
10
11
12 91

14 92 **2. Materials and methods**

16 93 *2.1. Materials*

18 94 Monoolein (MO, 1-monooleoylglycerol, RYLO MG 19 PHARMA, glycerol monooleate, 98.1
19
20 95 wt%) was kindly provided by Danisco A/S, DK-7200, Grinsted, Denmark. Pluronic F108 (PEO₁₃₂-
21
22 96 PPO₅₀-PEO₁₃₂), Docetaxel ($\geq 97\%$), N-hydroxysuccinimide (NHS, 98%), N,N'-
23
24 97 dicyclohexylcarbodiimide (DCC, $\geq 99.5\%$), triethylamine ($\geq 99.5\%$) and dimethyl sulfoxide (\geq
25
26 98 99.7%) were purchased from Sigma-Aldrich. Distilled water passed through a Milli-Q water
27
28 99 purification system (Millipore) was used to prepare the samples.
29
30
31
32 100

34 101 *2.2. Sample preparation*

36 102 Monoolein-based cubosomes were prepared and stabilized by dispersing the appropriate amount of
37
38 103 MO in aqueous solutions of a 60/20/20 mixture of Pluronic F108 (PF108), folate-conjugated, and
39
40 104 rhodamine-conjugated PF108 (PF108/PF108-FA/PF108-R) using an ultrasonic processor (UP100H
41
42 105 by Dr. Hielscher, cycle 0.9, amplitude 90 %) for 10 min. Docetaxel doped cubosomes were
43
44 106 obtained by dispersing the drug in the melted lipids (at 37 °C) with the help of an ultrasonic bath
45
46 107 before mixing with the Pluronic solution. The sample volume was usually 4 mL with approximately
47
48 108 96.4 wt % of water, 3.3 wt % of MO and 0.3 wt % Pluronics mixture.
49
50
51
52 109

54 110 *2.3. Synthesis of rhodamine-conjugated PF108 (PF108-R)*

1
2
3 111 PF108-NH₂ (0.1976 g, 0.013 mmol), N-hydroxysuccinimide (NHS, 0.0125 g, 0.108 mmol), N,N'-
4
5 112 dicyclohexylcarbodiimide (DCC, 0.0188 g, 0.091 mmol), and N-(9-(2-(4-(3-
6
7 113 carboxypropanoyl)piperazine-1-carbonyl)benzyl)-6-(diethylamino)-3H-xanthen-3-ylidene)-N-
8
9 114 ethylethanaminium (**4**) (0.024 g, 0.039 mmol) were dissolved in 8 mL of anhydrous DMSO in the
10
11 115 presence of triethylamine (20 μ L). To precipitate DCU (dicyclohexylurea), 20 mL of deionized
12
13 116 water were added, and the mixture was then centrifuged and filtered to obtain a red limpid solution.
14
15 117 This was dialyzed (14 kDa MW cut-off membrane) for 3 days against ultrapure water, which was
16
17 118 changed every 2-6 hours. The resulting product was lyophilized for 1 day to remove all the residual
18
19 119 water. Yield: 63% (130.3 mg, 0.008 mmol); mp: 48-50 °C. ¹H-NMR (400 MHz, DMSO-d₆, 298 K):
20
21 120 δ H 1.045 (3H \times 50, -CH₃ of PPO), 1.17-1.33 (m, 3H \times 2, -N(CH₂-CH₃)₂), 2.66-2.69 (m, 4H \times 2,
22
23 121 aliphatic protons from rhodamine moiety), 3.29-3.55 (m, 3H \times 50, 4H \times 264, -CH₂-CH(CH₃)-O- of
24
25 122 PPO and -CH₂-CH₂-O- of PEO), 3.60-3.73 (m, 2H \times 2, -N(CH₂-CH₃)₂), 4.53-4.56 (m, 1H \times 2,
26
27 123 amidic -NH), 6.95-8.07 (m, 10H \times 2, aromatic protons). IR (solid state, cm⁻¹) ν = 2876 (s), 1584,
28
29 124 1635, 1714 (w).
30
31
32
33
34
35

36 126 2.4. Photophysical characterization

37
38 127 Cubosome dispersions were diluted with Milli-Q water (1:100) before performing the photophysical
39
40 128 measurements. The emission and excitation spectra were recorded with a Perkin Elmer LS 55
41
42 129 spectrofluorimeter. The fluorescence quantum yield on PF108-R was determined by using
43
44 130 Rhodamine 6G dissolved in EtOH as the reference standard ($\Phi_{\text{ref}} = 0.94$). The absorption spectra
45
46 131 were recorded on a Thermo Nicolet Evolution 300 spectrophotometer.
47
48
49
50 132

51 133 2.5. Cryogenic transmission electron microscopy (cryo-TEM)

52 134 Vitrified specimens were prepared in a controlled environment vitrification system (CEVS) at 25 °C
53
54 135 and 100 % relative humidity. A drop (\sim 3 μ L) of the sample was placed on a perforated carbon
55
56 136 film-coated copper grid, blotted with filter paper, and plunged into liquid ethane at its freezing
57
58
59
60

1
2
3 137 point. The vitrified specimens were transferred to a 626 Gatan cryo-holder and observed at 120 kV
4
5 138 acceleration voltage in an FEI Tecnai T12 G² transmission electron microscope at about -175 °C in
6
7 139 the low-dose imaging mode to minimize electron-beam radiation-damage. Images were digitally
8
9 140 recorded with a Gatan US1000 high-resolution CCD camera.
10

11 141

12
13
14 142 *2.6. Small-angle x-ray scattering (SAXS)*

15
16
17 143 The characterization of the nanoparticles structure as a function of temperature was carried out by
18
19 144 SAXS using a Ganesha 300XL (SAXSLAB ApS, Skovlunde, Denmark). This instrument is
20
21 145 equipped with a 2D 300 K Pilatus detector (Dectris Ltd., Baden, Switzerland) and a Genix 3D X-
22
23 146 ray source (Xenocs SA, Sassenage, France), generating x-rays at a wavelength, λ , of 1.54 Å. The
24
25 147 scattering data was collected at a q -range of $0.014 < q \text{ (Å}^{-1}\text{)} < 0.753$, where the magnitude of the
26
27 148 scattering vector, q , is defined as $q = (4\pi/\lambda) \sin (\theta/2)$, where θ is the scattering angle. The two-
28
29 149 dimensional scattering pattern was radially averaged using SAXSGui software to obtain $I(q)$.
30
31 150 Measurements were performed in 1.5 mm quartz capillaries (Hilgenberg GmbH, Malsfeld,
32
33 151 Germany). The temperature was controlled by an external, recirculating water bath within ± 0.3 °C.
34
35 152 Samples were equilibrated during 1 hour at the measurement temperature prior performing the
36
37 153 experiment.
38
39

40
41 154 Water channels radii of the reverse bicontinuous cubic phases were calculated using the relation r_w
42
43 155 = $[(A_0/-2\pi\chi)^{1/2}a] - L$, where L is the length of the lipid hydrophobic chain (17 Å, in case of MO), a
44
45 156 is the lattice parameter obtained from the SAXS analysis, and A_0 and χ are the surface area and the
46
47 157 Euler characteristic (integral Gaussian curvature scaled by 2π) of the Infinite Periodic Minimal
48
49 158 Surface geometries within the unit cell, explained further in the Appendix ($Pn\bar{3}m$, $A_0 = 1.919$, $\chi =$
50
51 159 $- 2$; $Im\bar{3}m$, $A_0 = 2.345$, $\chi = - 4$). At least two Bragg peaks were used to estimate the errors
52
53 160 associated with a and r_w , unless otherwise indicated.
54
55
56

57 161
58
59
60

162 2.7. Light scattering

163 Dynamic light scattering (DLS) experiments were performed to obtain the size evolution of the
164 nanoparticles as a function of temperature. For that we used a light scattering goniometer
165 instrument (3D LS Spectrometer, LS Instruments, Fribourg, Switzerland), equipped with a 35 mW
166 He-Ne laser light source (wavelength of 632.8 nm). The instrument implements the so-called cross-
167 correlation scheme to suppress contributions from multiple scattering³²⁻³⁴ together with a
168 modulation unit.³⁵ The samples were placed in a 10 mm diameter cylindrical borosilicate disposable
169 culture tubes (Fisherbrand, Thermo Fisher Scientific Inc., Waltham, USA) and kept at the
170 measurement temperature in a temperature-controlled index-matching bath. Samples were
171 equilibrated at the measurement temperature for 10 minutes before the experiment. Measurements
172 were performed at a range of scattering angles between 40° and 100° (in triplicate at each scattering
173 angle). The initial decay rate, Γ , was derived from the second-order cumulant analysis of the
174 normalized field autocorrelation function, which was used to calculate the apparent collective
175 diffusion coefficient, D_0 , of the nanoparticles:

$$176 \Gamma = D_0 q^2 \quad (1)$$

177 where q is the module of the scattering vector, $q = (4\pi n/\lambda)\sin(\theta/2)$, with n the refractive index of
178 the solvent, λ the wavelength of the incoming laser light and θ the scattering angle. The
179 hydrodynamic radius, R_h , was obtained by the Stokes-Einstein relation ($D_0 = k_B T/6\pi\eta R_h$), where k_B
180 is the Boltzmann constant, T is the absolute temperature and η is the viscosity of the solvent at the
181 temperature T .

183 2.8. Cell Culture

184 HeLa cells (ATCC collection) were grown in phenol red-free Dulbecco's modified Eagle's medium
185 (DMEM, Molecular Probes, USA) with high glucose concentration, supplemented with 10 % (v/v)
186 fetal bovine serum, penicillin (100 U mL⁻¹) and streptomycin (100 μ g mL⁻¹) (Invitrogen) in 5% CO₂

1
2
3 187 incubator at 37 °C. Cells were seeded in 35 mm dishes; experiments were carried out two days after
4
5 188 seeding, when cells reached 90 % confluency. Liquid crystalline nanoparticles were added to the
6
7 189 cells at a concentration of 1: 500 (2 µL in 1 mL of fresh medium) and incubated at 37 °C for 4 h.
8
9
10 190 For live cell imaging, fresh serum-free medium was used to remove the extracellular particle
11
12 191 suspension before imaging session.

13 192

14
15
16 193 *2.9. Fluorescence microscopy*

17
18
19 194 Light microscopy observations were made using a Zeiss (Axioskop) upright fluorescence
20
21 195 microscope (Zeiss, Oberkochen, Germany) equipped with 10x, 20x and 40x/0.75 NA water
22
23 196 immersion objectives and a HBO 50 W L-2 mercury lamp (Osram, Berlin, Germany). Twelve-bit-
24
25 197 deep images were acquired with a monochrome cooled CCD camera (QICAM, Qimaging, Canada).
26
27 198 For observation of dye fluorescence, filters were: ex 546 ± 6 nm, em 620 ± 60 nm. Digital images
28
29 199 were obtained with Image Pro Plus software (Media Cybernetics, Silver Springs, MD).

30
31
32 20033
34
35
36 201 *2.10. Cytotoxic activity (MTT assay)*

37
38 202 The cytotoxic effect of cubosome formulations was evaluated in HeLa cells by the MTT assay.
39
40 203 HeLa cells were seeded in 24-well plates at density of 3×10^4 cells/well in 500 µL of serum-
41
42 204 containing media. Experiments were carried out two days after seeding when cells had reached 90
43
44 205 % confluence. The different formulations were added to the cells at concentration of 1:500 (2 µL in
45
46 206 1 mL of serum-free medium) and incubated at 37 °C for 4 h. The effect of Docetaxel 10 µM
47
48 207 (specifically, 1 µL of a 10 mM solution of Docetaxel in DMSO was added to 1 mL of serum-free
49
50 208 medium) on HeLa cell viability was also tested for comparison at the same incubation time. A 50
51
52 209 µL portion of MTT solution (3-(4,5-dimethylthiazol-2-yl)-2,5-diphenyltetrazolium bromide) (5
53
54 210 mg/mL in H₂O), was then added and left for 2 h at 37 °C. The medium was aspirated, 500 µL of
55
56 211 DMSO was added to the wells, and color development was measured at 570 nm with an Infinite 200
57
58
59
60

1
2
3 212 auto microplate reader (Infinite 200, Tecan, Austria). The absorbance is proportional to the number
4
5 213 of viable cells. All measurements were performed in quadruplicate and repeated at least three times.
6
7 214 Results are shown as percent of cell viability in comparison with non-treated control cells. Data
8
9 215 were expressed as a mean \pm standard deviation (SD) of three independent experiments involving
10
11 216 quadruplicate analyses for each sample.
12
13
14 217

16 218 *2.11. Determination of MO and Docetaxel content in cubosomes*

18 219 After loading with Docetaxel, the cubosome dispersion was purified from the non-encapsulated
19
20 220 drug by dialysis: 2 mL were loaded into a dialysis tubing cellulose membrane (14 kDa MW cutoff)
21
22 221 and dialyzed against water (1000 mL), for 2 h (by replacing the water after 1 hour) at 25 °C. It
23
24 222 should be noticed that this purification step did not influence the concentration of the dye in the
25
26 223 formulation since the fluorophore-conjugated PF108 has a MW higher than the membrane cutoff
27
28 224 (about 16 kDa). Therefore, in comparison with traditional methods that require enclosing the dye
29
30 225 within the lipid bilayer, this new procedure allows a huge saving of the (typically very expensive)
31
32 226 dye. Aliquots (10 μ L) of the nanoparticle preparations were dissolved in 300 μ L of CH₃CN with
33
34 227 0.14 % CH₃COOH (v/v). The samples were vortexed to obtain a clear solution, and aliquots (20 μ L)
35
36 228 were injected into the Agilent Technologies 1100 liquid chromatograph (Agilent Technologies, Palo
37
38 229 Alto, CA) equipped with a diode array detector (DAD). Analyses of MO (detected at 200 nm) and
39
40 230 Docetaxel (at 230 nm) in nanoparticle dispersions were carried out with a XDB-C₁₈ Eclipse (150 ´
41
42 231 4.6 mm, 3.5 mm particle size) (Agilent Technologies) equipped with a Zorbax XDB-C₁₈ Eclipse
43
44 232 (12.5 ´ 4.6 mm, 5 mm particle size) guard column (Agilent Technologies), with a mobile phase of
45
46 233 CH₃CN/H₂O/CH₃COOH (75/25/0.12, v/v/v), at a flow rate of 2.3 mL/min. The temperature of the
47
48 234 column was maintained at 37 °C. Recording and integration of the chromatogram data was carried
49
50 235 out through an Agilent OpenLAB Chromatography data system. The identification of lipid
51
52 236 components and drug was made using standard compounds and conventional UV spectra.
53
54
55
56
57
58
59
60

1
2
3 237 Calibration curves of all of the compounds were constructed using standards and were found to be
4
5 238 linear, with correlation coefficients > 0.995 .

7 239 Drug encapsulation efficacy (EE%) was calculated by the following equation:³⁶ $EE\% = (\text{weight of}$
8
9 240 $\text{the drug in nanoparticles})/(\text{weight of the feeding drug}) \times 100 \%$. Data were expressed as a mean \pm
10
11 241 standard deviation (SD) of three independent experiments involving duplicate analyses for each
12
13 242 sample.

14
15
16 243

18 244 *2.12. Statistical analysis*

20
21 245 Evaluation of statistical significance of differences was performed using Graph Pad INSTAT
22
23 246 software (GraphPad software, San Diego, CA, USA). Comparison between groups was assessed by
24
25 247 one-way analysis of variance (One-way ANOVA) followed by the Bonferroni Multiple
26
27 248 Comparisons Test.

28
29
30 249

31 250 **3. Results**

33 251 *3.1. Synthesis of rhodamine-conjugated PF108 and liquid crystalline nanoparticles* 34 35 36 252 *characterization*

37
38 253 When designing a nanoparticle for diagnostic or theranostic applications, two different approaches
39
40 254 could be adopted: one is doping the nanoparticle with the imaging agent (a fluorescent probe, for
41
42 255 instance); the other is functionalizing the nanoparticle with the imaging agent. This approach is
43
44 256 quite straightforward in the case of silica-based nanoparticles, which can be easily functionalized by
45
46 257 well-established siloxane chemistry.³⁷ Functionalization of nanoparticles as the cubosomes reported
47
48 258 here, can efficiently be achieved conjugating the amphiphilic polymers used to stabilize the
49
50 259 formulation (Pluronic F108, PF108, in our case) with a suitably chemically modified imaging
51
52 260 agent.³⁸ Here, the fluorogenic molecule rhodamine B was conjugated to PF108 via a multi-steps
53
54 261 approach (see Scheme 1). First the fluorophore was synthetically modified as reported in literature³⁹
55
56 262 to obtain its piperazine amide derivative (**4**) that was subsequently conjugated to the aminated
57
58
59
60

1
2
3 263 derivative of the PF108.⁴⁰ The reaction was carried out in DMSO in the presence of DCC, NHS and
4
5 264 Et₃N. Then, the product was dialyzed against deionized water, and lyophilized.

6
7 265 Since the folate receptor is overexpressed on cancer cell membrane, the PF108 was also conjugated
8
9 266 with folic acid as previously reported²⁰ to actively target the nanoparticles towards cancer tissues.

10
11 267 A mixture of the commercial PF108, folate-conjugated PF108 (PF108-FA), and rhodamine-
12
13 268 conjugated PF108 (PF108-R) was used to formulate cubosome dispersions in water also loaded
14
15 269 with the anticancer drug Docetaxel (DTX). According to preliminary tests, it was found that a
16
17 270 mixture having the ratio PF108/PF108-FA/PF108-R = 60/20/20 (wt %) suitably stabilizes the
18
19 271 dispersion for more than two months. This formulation was then investigated for its morphological
20
21 272 and structural aspects by cryo-TEM, SAXS, and DLS measurements.

22
23 273 Figure 1 shows a typical cryo-TEM image of the cubosome formulation we proposed. Close
24
25 274 inspection of the image in Figure 1 reveals a number of spherical cubosomes of different sizes and
26
27 275 an inner structure characterized by a dark matrix and alternate bright spots, respectively
28
29 276 representing the lipid bilayer and the water channels. As often occurs, some vesicular materials can
30
31 277 be seen attached to the liquid crystalline nanoparticles while, differently from other cubosome
32
33 278 formulations, only a few vesicles are noticed. Indeed, unilamellar or oligolamellar vesicles typically
34
35 279 form during the process of cubosome production, very likely because of the presence of the
36
37 280 Pluronic used as dispersant (MO in water does not produce small uni-lamellar or oligo-lamellar
38
39 281 vesicles).⁴¹ Actually, depending on the method of preparation, vesicles may exceed cubosomes in
40
41 282 terms of number density.⁴² Therefore, the absence of vesicular material observed here could be
42
43 283 ascribed to the use of the conjugated Pluronics as stabilizer for the cubosome formulation.

44
45 284 Taking into account the possible use of the system under study as theranostic nanocarrier, variation
46
47 285 of size and inner structure upon temperature changes were monitored through DLS and SAXS
48
49 286 measurements in the range 10-50 °C. Particularly, the temperatures were chosen to include two
50
51 287 extreme storage temperatures (10 and 50 °C) as well as room and physiological temperatures.
52
53 288 Moreover, to find out if the system nanostructure after temperature cycling is reestablished, SAXS
54
55
56
57
58
59
60

289 measurements were performed in the following order: 25, 37, 50, 10, 25, and 37 °C. Results are
 290 reported in Figure 2 and Table 1.

291

292 Table 1. Cubosome lattice parameters (a) and radius of the water channels (r_w). Experiments were
 293 performed at different temperatures in the order reported in the table.

T (°C)	<i>Pn</i> <u>3</u> <i>m</i>		<i>Im</i> <u>3</u> <i>m</i> ^a	
	a (Å)	r_w (Å)	a (Å)	r_w (Å)
25	97.0 ± 0.5	20.9 ± 0.2	129.6	22.6
37	89.2 ± 0.2	17.9 ± 0.1	118.7	19.3
50	80.7 ± 0.2	14.5 ± 0.1	109.6	16.5
25	97.1 ± 0.6	21.2 ± 0.3	123.1	20.6
37	90.5 ± 0.7	18.4 ± 0.3	118.7	19.3

294 ^a Standard deviations on a and r_w pertaining to *Im*3*m* phase were not reported since these
 295 parameters were obtained from the single Bragg peak discernible in the diffraction pattern.

296

297 SAXS results confirmed the bicontinuous cubic inner structure of the formulation. Actually, the
 298 diffraction pattern of the cubosome formulation at 25 °C (Figure 2) is dominated by four Bragg
 299 peaks placed in a q ratio of $\sqrt{2}:\sqrt{3}:2:\sqrt{6}$ that clearly identify the double diamond (*Pn*3*m*)
 300 bicontinuous cubic phase. However, a weak reflection at low q reveals the simultaneous presence of
 301 the primitive (*Im*3*m*) bicontinuous cubic phase. The coexistence of the *Pn*3*m* and the *Im*3*m*
 302 phases in cubosome formulations is widely reported in literature; it is attributed to a *Pn*3*m* to
 303 *Im*3*m* intercubic phase transition caused by the interaction of the hydrophobic moiety of the
 304 Pluronic with the surface of the cubosome nanoparticles.⁴³

305 The lattice parameter, a , obtained from the SAXS experiments performed at different temperatures
 306 along with the calculated radius of the water channels r_w (see paragraph 2.3) are reported in Table 1.

1
2
3 307 As usually detected in liquid crystalline systems, although the nanostructure is retained, the lattice
4
5 308 parameter (and consequently the radius of the water channels) of the cubosomes decreases while the
6
7 309 temperature increases in the sequence 25, 37, 50 °C. This phenomenon is related to the enhanced
8
9 310 disorder of the lipid chain at higher temperatures that, in turn, induces higher negative curvature at
10
11 311 the lipid/water interface.⁴³ The disappearance of the weaker Bragg peaks detected in the diffraction
12
13 312 patterns obtained at 10 °C (see Figure 2) indicates that the inner structure is in some way altered,
14
15 313 although not completely lost. When the temperature is raised again to 25 or 37 °C the nanostructure
16
17 314 is recovered. However some significant differences can be noticed in the intensity of the Bragg
18
19 315 peaks and the general appearance of the diffractograms after the temperature cycle. Therefore, it can
20
21 316 be concluded that while the nanostructure is reestablished, the system evolution upon temperature
22
23 317 changes is characterized by a certain degree of hysteresis.

24
25 318 The overall trend described by the DLS measurements of the nanoparticles hydrodynamic radius
26
27 319 can be extrapolated from results reported in Table 2. Essentially, the nanoparticle average size does
28
29 320 not vary significantly upon temperature changes.
30
31
32
33

34 321

35
36 322 Table 2. Average hydrodynamic radius (R_h) and polydispersity index (PdI) of the cubosome
37
38 323 formulation at different temperatures.

T (°C)	R_h (nm)	PdI
10	85	0.13
25	90	0.16
37	88	0.14
50	87	0.21

39
40
41
42
43
44
45
46
47
48
49
50
51
52 324

53
54 325 *3.2. Rhodamine-conjugated liquid crystalline nanoparticles photophysical characterization and*
55
56 326 *HeLa cells imaging*
57
58
59
60

1
2
3 327 The photophysical properties of PF108-R, as well as those of cubosomes, were investigated.
4
5 328 Rhodamine dyes belong to the class of xanthene dyes, characterized by an intense red fluorescence,
6
7 329 high brightness, excellent photostability, and the ability to modulate the properties of the dye
8
9 330 through substitution.⁴⁴ A key property of these dyes is the equilibrium between an open, colored,
10
11 331 fluorescent quinoid form or a closed, colorless, nonfluorescent lactone, which can be controlled by
12
13 332 appropriate substitution.⁴⁵ In particular, rhodamine B (bearing two diethyl amino substituents) is
14
15 333 one of the most common derivative.
16
17
18 334 The emission/absorption properties of PF108-R were investigated in water and chloroform to test its
19
20 335 photophysical features in media of different polarities. In both solvents the PF108-R has a strong
21
22 336 absorption band at 560 nm ($\epsilon = 30660 \text{ M}^{-1}\text{cm}^{-1}$, $31770 \text{ M}^{-1}\text{cm}^{-1}$ in water and chloroform,
23
24 337 respectively) and a shoulder at 522 nm ($\epsilon = 13100 \text{ M}^{-1}\text{cm}^{-1}$, $9950 \text{ M}^{-1}\text{cm}^{-1}$ in water and chloroform,
25
26 338 respectively). Upon excitation at 522 nm in water, an emission band at 594 nm is generated.
27
28 339 Conversely, the excitation at the same wavelength in chloroform generates a strong emission band
29
30 340 at 584 nm. The quantum yields measured were 0.16 and 0.58 respectively in water and chloroform.
31
32 341 As expected, water has a quenching effect on the rhodamine fluorescence. The shift of the emission
33
34 342 to higher energy could be explained considering the solvatochromic properties of the fluorophore.
35
36 343 The emission spectrum of the cubosome formulation stabilized with the PF108/PF108-FA/PF108-R =
37
38 344 60/20/20 (wt %) mixture was also recorded after 1:100 dilution in water. Excitation at 522 nm resulted in
39
40 345 emission bands centered at 581 nm (see Figure 3). The position of the maximum emission wavelength is
41
42 346 similar to that observed for PF108-R in chloroform. These results suggest that the rhodamine fragment
43
44 347 conjugated to the Pluronic F108, rather than protruding towards the bulk water, is hidden within the
45
46 348 polyethylenoxide corona surrounding the nanoparticle, thus experiencing a less polar environment. The
47
48 349 excitation spectrum of cubosomes is in accordance with PF108-R absorption both in water and chloroform.
49
50 350 Due to the turbidity of the solution the determination of the quantum yield of the dye in the nanoparticles
51
52 351 was not possible.
53
54
55
56
57
58
59
60

1
2
3 352 The uptake of cubosome nanoparticles was investigated by fluorescence microscopy. After 4 h incubation,
4
5 353 faint diffuse fluorescence was distributed within cytoplasm of HeLa cells, whereas in untreated-control cells
6
7 354 no fluorescence was detected (Figure 4). However, it was not possible to determine whether the dye
8
9 355 molecules were localized in specific cell compartments.
10

11 356

12

13 357 *3.3. Monoolein and Docetaxel level in cubosome formulations and cytotoxic activity (MTT assay)*

14

15 358 The amount of MO (expressed as mg/mL of dispersion) and Docetaxel (DTX, $\mu\text{g/mL}$) in different
16
17 359 cubosome formulations was monitored by HPLC. The formulations analyzed were the traditional
18
19 360 cubosomes formulation stabilized with PF108 (CUB), the cubosomes formulation stabilized with
20
21 361 the PF108/PF108-FA/PF108-R = 60/20/20 (wt %) mixture (CUB-R), and the latter formulation also
22
23 362 loaded with DTX (CUB-R/DTX).
24
25

26 363 Monoolein content in CUB, CUB-R, and CUB-R/DTX formulations was 33 ± 3 , 35 ± 2 , and 29 ± 2
27
28 364 mg/mL, respectively. The CUB-R/DTX formulation was loaded with $328 \pm 25 \mu\text{g/mL}$ of drug, with
29
30 365 a DTX/MO molecular ratio of 1/200. The encapsulation efficacy (EE%) was $103 \pm 13 \%$.
31
32

33 366 These formulations were tested for cytotoxicity (MTT assay) in HeLa cells. Figure 5 shows the
34
35 367 viability, expressed as % of the control, induced in HeLa cancer cells in the presence of the
36
37 368 nanoparticle formulations at concentration 1:500 ($2 \mu\text{L/mL}$ of medium) after 4 h of incubation. The
38
39 369 cytotoxic effect of DTX $10 \mu\text{M}$ (see paragraph 2.10) was also determined at 4 h-incubation for
40
41 370 comparison. Treatment with CUB and CUB-R formulations did not induce a significant reduction
42
43 371 in cell viability, in comparison with control cells (Ctrl). Differently, the incubation with CUB-
44
45 372 R/DTX particles induced a statistically significant decrease in HeLa cell viability (36 % of
46
47 373 reduction) with respect to the control as a result of the presence of the anticancer drug. A significant
48
49 374 cytotoxic effect (27 % reduction in cell viability) was also observed in cells treated with the
50
51 375 anticancer drug (DTX) directly added to the cell culture. Remarkably, the HeLa cell treatment with
52
53 376 DTX-loaded cubosomes (DTX dose of approximately $0.8 \mu\text{M}$) induced a superior cytotoxic effect
54
55
56
57
58
59
60

1
2
3 377 compared to the molecularly dispersed anticancer drug tested at much higher (12.5-fold)
4
5 378 concentration.

7 379 DTX is one of the most effective anticancer agents and has activity against a wide range of cancers.
8
9 380 The growth inhibitory effect of DTX was examined in several cancer cell lines and the IC₅₀ (50%
10
11 381 inhibitory concentration) values of this taxoid were in the nanomolar range at long-time incubation
12
13 382 (72 h)^{46,47} The 24 and 48 h IC₅₀ values of the free DTX in HeLa cells were previously found to be
14
15 383 5.01 and 2.62 μg/mL, respectively.⁴⁸ Here, the higher cytotoxicity at 4 h-incubation of DTX
16
17 384 administered via the nanoparticles (0.66 μg/mL) with respect to free drug molecules (8.08 μg/mL)
18
19 385 can be explained calling into play different uptake mechanisms. Indeed, cubosomes can deliver
20
21 386 DTX into cells via endocytosis, while free DTX can enter cells via passive diffusion with inherent
22
23 387 lipophilicity, and various ABC efflux transporters, expressed at the cellular membrane, can
24
25 388 minimize its effective penetration by efficiently eliminating the drug from the cell.⁴⁹
26
27
28
29
30
31

32 390 *3.4 Cubosomes versus multi-lamellar liposome hydrophobic volume*

33 391 One important feature that distinguishes cubosomes (reverse bicontinuous cubic liquid crystalline
34
35 392 nanoparticles) from liposomes (their lamellar counterpart) is the higher hydrophobic volume of the
36
37 393 former. Since cubosomes are mainly proposed as nanocarriers for hydrophobic molecules of
38
39 394 pharmaceutical interest as an alternative to liposomes, this fact may be extremely relevant in view
40
41 395 of their theranostic applications. Given the very convoluted volumes occupied by lipid chains in
42
43 396 bicontinuous morphologies compared with the shells of liposomes, it is tempting to assume that the
44
45 397 former contains a far larger hydrophobic volume (suitably) normalized than the latter. Surprisingly,
46
47 398 quantification of the hydrophobic volumes of bicontinuous cubosomes with respect to multi-
48
49 399 lamellar liposomes has never been reported.

50
51 400 Assume for simplicity that we have two nanoparticles composed of monoolein in water whose outer
52
53 401 diameter is 100 nm. Assume the liposome is composed of N concentric spherical monoolein
54
55
56
57
58
59
60

1
2
3 402 bilayers, composed of pairs of monolayers, each with hydrophobic thickness of 17 Å, corresponding
4
5 403 to the likely chain length in molten monoolein assemblies. Further, assume that adjacent bilayers
6
7 404 are separated by polar films 16 Å thick, so that each monolayer has an associated polar layer of
8
9 405 thickness of 8 Å (corresponding to dimensions in the fully hydrated lamellar mesophase).⁵⁰ Each
10
11 406 repeat unit of chains, monoolein head-groups, and water is therefore 50 Å thick. The hydrophobic
12
13 407 volume is then calculated as the chain contribution to the total volume within N concentric nested
14
15 408 shells, whose outermost radius is scaled such that the outermost monolayer and associated polar
16
17 409 layer has diameter of 100 nm. These dimensions imply that the hydrophobic volume fraction within
18
19 410 the liposome (whose total volume is $5.24 \times 10^5 \text{ nm}^3$) is approximately 0.18, 0.33, 0.445, 0.53, 0.59
20
21 411 nm^3 for $N = 1, 2, 3, 4, 5$ bilayers, respectively. The exposed outermost monolayer has area $2.83 \times$
22
23 412 10^4 nm^2 .

24
25
26
27 413 The structural dimensions of a typical cubosome can be estimated as follows. We assume the
28
29 414 cubosome is a single crystalline domain of the $Im\bar{3}m$ phase, also contained within a spherical shell
30
31 415 of diameter 100 nm (cubosome nanoparticles, although characterized by a cubic inner
32
33 416 nanostructure, can be spherical in shape, as those shown in Fig. 1). We choose a typical lattice
34
35 417 dimension of the $Im\bar{3}m$ unit cell, namely 130 Å, and fix the chain length to be the same as that in
36
37 418 the liposome, 17 Å (the polar dimensions are then fixed by those parameters). The resulting total
38
39 419 exposed area is then $1.68 \times 10^5 \text{ nm}^2$ (equal to the summed area of each monolayer displaced 17 Å
40
41 420 from the bilayer mid-surface, whose geometry is assumed to lie on the P-surface, the cubic periodic
42
43 421 $Im\bar{3}m$ minimal surface). Surprisingly, the membrane area exposed to water in the liposome is
44
45 422 substantially larger than the total area in the cubosome. The corresponding hydrophobic volume
46
47 423 fraction within the 100 nm cubosomal sphere is 0.59 nm^3 , higher than that of the liposome with up
48
49 424 to 5 bilayers (see Table 3).
50
51
52
53
54
55
56
57
58
59
60

1
2
3 426 Table 3. Cubosome-to-liposome hydrophobic volume ratios (V_h) as a function of the number of
4
5 427 concentric bilayers in the liposome (see also the text).
6

Number of bilayers	1	2	3	4	5
V_h ratios	3.22	1.79	1.33	1.12	1.00

7
8
9
10
11
12 428

13 14 429 **4. Conclusion**

15
16 430 In this paper we demonstrated that cubosomes loaded with an anticancer drug, namely Docetaxel,
17
18 431 can be formulated decorating their nanoparticle surface with both a cancer cell targeting ligand and
19
20 432 an imaging probe. Worth noticing, this is the first time that Docetaxel is successfully loaded within
21
22 433 cubosomes, and that cubosomes surface is simultaneously decorated with targeting and imaging
23
24 434 moieties. To this aim, the commercial block copolymer Pluronic F108 (PF108), and its folate- and
25
26 435 rhodamine-conjugated counterparts were used in a 60/20/20 (wt %) mixture to stabilize the lipid
27
28 436 liquid crystalline dispersion. SAXS, DLS and cryo-TEM investigation, at the temperatures range
29
30 437 explored, confirmed the cubic bicontinuous inner structure of the nanoparticles and showed the
31
32 438 physicochemical aspects (morphology and size) akin to those of traditionally prepared cubosome
33
34 439 dispersions. Photophysical measurements suggested that the fluorogenic fragment, although
35
36 440 conjugated to the terminal ethylenoxide moiety of PF108, was very likely exposed to the less polar
37
38 441 environment constituted by the polyethylenoxide corona surrounding the nanoparticles, rather than
39
40 442 protruded toward the bulk water. This formulation, not loaded with the drug, was successfully used
41
42 443 to image living HeLa cells. Besides, viability tests revealed a significant cytotoxic effect (more than
43
44 444 one order of magnitude larger than the molecularly dispersed drug) of the Docetaxel loaded
45
46 445 nanoparticles against HeLa cells. These results evidenced that loading of cubosomes with a
47
48 446 Docetaxel dose able to induce cytotoxic effects on HeLa cells and decoration of their surface with
49
50 447 40% of conjugated PF108 did not compromise the intrinsic nature of these peculiar nanoparticles
51
52 448 and their cellular uptake. We have also evaluated the differences between cubosomes and multi-
53
54 449 lamellar liposomes in terms of surface area and hydrophobic volume. Under the imposed constraints
55
56
57
58
59
60

1
2
3 450 (same molecular building block and nanoparticles volume, cubosome nanostructure characterized
4
5 451 by the $Im\bar{3}m$ space group with a lattice parameter of 130 Å, and multi-lamellar liposome
6
7 452 constituted of adjacent bilayers), these calculations demonstrated that the hydrophobic volume of
8
9 453 cubosomes is more than three times larger than that of single-bilayer liposomes, but the cubosome
10
11 454 to liposome hydrophobic volume ratio rapidly converge to unity as the number of the bilayers in the
12
13 455 liposome increases. It is worth noting that this ratio will be even larger if the liposome contains non-
14
15 456 adjacent bilayers. Remarkably, the cubosome surface exposed to water is about 60 % with respect
16
17 457 to that of the liposome.

18
19
20
21 458 Taken together, these findings demonstrate the good performance of cubosomes as peculiar
22
23 459 nanocarriers for hydrophobic molecules with therapeutic/diagnostic relevance, and encourage the
24
25 460 investigation of cubic bicontinuous liquid crystalline dispersion for possible applications as
26
27 461 theranostic tools.

28
29
30 462

31 463 **5. Appendix: Geometric calculations**

32
33
34 464 Denote the chain length by d , t the thickness of the polar layer (containing water plus head groups)
35
36 465 and the lattice parameter in the cubic mesophase by a . Assume that outer shape of the liposome and
37
38 466 the cubosome is a sphere of outer diameter L .

39
40
41 467 We assume that all interfaces, lining the monolayers at the chain-water interface and the free chain
42
43 468 ends, are parallel. We then use the formalism described elsewhere¹ to deduce dimensions. All
44
45 469 dimensions are calculated from the geometry of the imaginary surface S that run between the chain
46
47 470 ends in opposed mono-layers, at the mid-section of the hydrophobic shell for each bilayer. The
48
49 471 “outer” surfaces, exposed to water, are parallel to S , and displaced by d from S . We have two
50
51 472 formulae derived from the geometry of parallel surfaces, both related to the mean and Gaussian
52
53 473 curvatures of S , denoted H_S and K_S respectively. One is for the area of the surface S_x , parallel to S ,
54
55 474 displaced by a distance x :

56
57
58
59 475
60

$$area(S_x) = area(S)(1 + 2Hx + Kx^2)$$

476

(where the sign of x depends whether it is on the outside or the inside of the surface). The second

describes the volume of the film lying-in between S and S_x :

479

$$volume(S_x) = area(S)x\left(1 + Hx + \frac{Kx^2}{3}\right)$$

480

In the liposome, those surfaces are parallel spheres, and if it is made of N bilayers, there are N such

spheres, each one with radius:

483

$$r(i) = \frac{L}{2} - (2i - 1)(d + t)$$

484

These dimensions impose mean and Gaussian curvatures on bilayer i equal to:

486

$$H(i) = r(i)^{-1}$$

$$K(i) = r(i)^{-2}$$

487

The exposed area of the liposome is that of the outermost spherical mono-layer (displaced distance t

inwards from the 100 nm external shell), namely $4\pi r(l)^2$. The total volume is $V_{total} = \frac{4}{3}\pi\left(\frac{L}{2}\right)^3$. The

hydrophobic (chain) volume in the liposome is determined by summing over all $2N$ monolayers, N

displaced x and N displaced $-x$:

492

$$volume(N) = 4\pi d \sum_{i=1}^N r(i)^2 \left\{ \left(1 + H(i)d + \frac{d^2}{3K(i)}\right) + \left(1 - H(i)d + \frac{d^2}{3K(i)}\right) \right\} \quad (1)$$

494

1
2
3 495 The corresponding calculation for the cubosome follows directly from the normalised surface to
4
5 496 volume ratio, or “homogeneity index” characteristic of a particular folded surface geometry:
6

7 497

$$\mathcal{H} := \frac{area_Q^{\frac{3}{2}}}{(-2\pi\chi)^{\frac{1}{2}} volume}$$

14 498

16
17 499 where χ is the Euler characteristic of the hyperbolic bilayer within the particle. If the cubosome is
18
19 500 contained within a spherical shell of diameter L and the membrane within folds onto a periodic
20
21 501 minimal surface forming a cubic lattice of lattice edge a , whose topology per unit cell is χ_0 , then

22
23
24 502 $\chi = \chi_0 \frac{V_{total}}{a^3}$. The radius of curvature of the minimal surface is given by the expression:
25

26 503

$$r_Q = \left\{ \frac{\mathcal{H}}{-2\pi\chi} \right\}^{\frac{1}{3}},$$

32 504

33
34
35 505 which corresponds to minimal surface curvatures $H_Q = 0$ and $K_Q = -r_Q^{-2}$.⁵⁰ It follows that the
36
37 506 minimal surface area in the cubosome,
38

39 507

$$area_Q = \left\{ \mathcal{H} V_{total} (-2\pi\chi)^{\frac{1}{2}} \right\}^{\frac{2}{3}},$$

45 508

46
47 509 so that the exposed area (at the hydrophobic/hydrophilic interface) is:
48

49 510

$$area_{exposed} = 2area_Q (1 - Kd^2),$$

54 511

55
56
57 512 and the hydrophobic volume is
58
59
60

513

$$514 \quad volume_Q = 2area_{exposed} \left(1 + \frac{d^3}{3K_Q} \right) \quad (2)$$

515

516 If the internal bilayer geometry within the cubosome corresponds to the $Im\bar{3}m$ bicontinuous
517 mesophase, the relevant data are $\mathcal{H} = 0.7163$ and $\chi_0 = -4$.⁵¹ The ratios of hydrophobic volumes
518 are calculated from the results of equations (1) and (2) above.

519

520 Acknowledgments

521 Karin Schillén and Tommy Nylander are kindly thanked for fruitful discussions. The authors
522 acknowledge financial support from the European Commission under the Seventh Framework
523 Program by means of the grant agreement for the Integrated Infrastructure Initiative N. 262348
524 European Soft Matter Infrastructure (ESMI). Financial support by MIUR (Project PRIN
525 2010BJ23MN_002), Fondazione Banco di Sardegna and Regione Autonoma della Sardegna (CRP-
526 59699) is gratefully acknowledged. Sardegna Ricerche Scientific Park (Pula, CA, Italy) is
527 acknowledged for free access to facilities of the Nanobiotechnology Laboratory. The cryo-TEM
528 work was performed at the Technion Laboratory for Electron Microscopy of Soft Matter, supported
529 by the Technion Russell Berrie Nanotechnology Institute (RBNI).

530

531 **References**

- 532 1. Hyde, S.; Andersson, S.; Larsson, K.; Blum, Z.; Landh, T.; Lidin, S.; Ninham, B. W. *The*
533 *Language of Shape*; Elsevier: Amsterdam, 1997; Vol. chap. 1-5.
- 534 2. Luzzati, V.; Husson, F. The structure of the liquid-crystalline phases of
535 lipid–water systems. *J. Cell Biol.* **1962**, *12*, 207–219.
- 536 3. Larsson, K. Cubic lipid-water phases: Structure and biomembrane aspects. *J. Phys. Chem.*
537 **1989**, *93*, 7304-7314.
- 538 4. Bender, J.; Ericson, M. B.; Merclin, N.; Iani, V.; Rosén, A.; Engström, S.; Moan, J. Lipid
539 cubic phases for improved topical drug delivery in photodynamic therapy. *J. Control. Release* **2005**,
540 *106*, 350-360.
- 541 5. Caboi, F.; Amico, G. S.; Pitzalis, P.; Monduzzi, M.; Nylander, T.; Larsson, K. Addition of
542 hydrophilic and lipophilic compounds of biological relevance to the monoolein/water system. I.
543 Phase behavior. *Chem. Phys. Lipids* **2001**, *109*, 47-62, and references therein.
- 544 6. Lopes, L. B.; Collett, J. H.; Bentley, M. V. L. B. Topical delivery of cyclosporin A: an in
545 vitro study using monoolein as a penetration enhancer. *Eur. J. Pharm. Biopharm.* **2005**, *60*, 25-30.
- 546 7. Monduzzi, M.; Lampis, S.; Murgia, S.; Salis, A. From self-assembly fundamental
547 knowledge to nanomedicine developments. *Adv. Colloid Interface Sci.* **2014**, *205*, 48-67.
- 548 8. Murgia, S.; Caboi, F.; Monduzzi, M. Addition of hydrophilic and lipophilic compounds of
549 biological relevance to the monoolein/water system II — ¹³C NMR relaxation study. *Chem. Phys.*
550 *Lipids* **2001**, *110*, 11-17.
- 551 9. Mulet, X.; Boyd, B. J.; Drummond, C. J. Advances in drug delivery and medical imaging
552 using colloidal lyotropic liquid crystalline dispersions. *J. Colloid Interface Sci.* **2013**, *393*, 1-20.
- 553 10. Chong, J. Y. T.; Mulet, X.; Postma, A.; Keddie, D. J.; Waddington, L. J.; Boyd, B. J.;
554 Drummond, C. J. Novel RAFT amphiphilic brush copolymer steric stabilisers for cubosomes:
555 poly(octadecyl acrylate)- block-poly(polyethylene glycol methyl ether acrylate). *Soft Matter* **2014**,
556 *10*, 6666–6676.

- 1
2
3 557 11. Chong, J. Y. T.; Mulet, X.; Waddington, L. J.; Boyd, B. J.; Drummond, C. J. High-
4
5 558 Throughput Discovery of Novel Steric Stabilizers for Cubic Lyotropic Liquid Crystal Nanoparticle
6
7 559 Dispersions. *Langmuir* **2012**, *28*, 9223–9232.
- 8
9
10 560 12. Johnsson, M.; Barauskas, J.; Norlin, A.; Tiberg, F. Physicochemical and drug delivery
11
12 561 aspects of lipid-based liquid crystalline nanoparticles: a case study of intravenously administered
13
14 562 propofol. *J. Nanosci. Nanotechnol.* **2006**, *6*, 3017–3024.
- 15
16 563 13. Esposito, E.; Ravani, L.; Mariani, P.; Contadod, C.; Drechsler, M.; Puglia, C.; Cortesi, R.
17
18 564 Curcumin containing monoolein aqueous dispersions: A preformulative study. *Mater. Sci. Eng.*
19
20 565 **2013**, *33*, 4923–4934.
- 21
22
23 566 14. Fraser, S. J.; Rose, R.; Hattarki, M. K.; Hartley, P. G.; Dolezal, O.; Dawson, R. M.;
24
25 567 Separovica, F.; Polyzos, A. Preparation and biological evaluation of self-assembled cubic phases for
26
27 568 the polyvalent inhibition of cholera toxin. *Soft Matter* **2011**, *7*, 6125-6134.
- 28
29 569 15. Montis, C.; Castroflorio, B.; Mendoza, M.; Salvatore, A.; Berti, D.; Baglioni, P.
30
31 570 Magnetocubosomes for the delivery and controlled release of therapeutics. *J. Colloid Interface Sci.*
32
33 571 **2015**, *449*, 317-326.
- 34
35
36 572 16. Rattanapak, T.; Birchall, J.; Young, K.; Ishii, M.; Meglinski, I.; Rades, T.; Hook, S.
37
38 573 Transcutaneous immunization using microneedles and cubosomes: Mechanistic investigations using
39
40 574 Optical Coherence Tomography and Two-Photon Microscopy. *J. Control. Release* **2013**, *172*, 894–
41
42 575 903.
- 43
44
45 576 17. Rizwan, S. B.; McBurney, W. T.; Young, K.; Hanley, T.; Boyd, B. J.; Rades, T.; Hook, S.
46
47 577 Cubosomes containing the adjuvants imiquimod and monophosphoryl lipid A stimulate robust
48
49 578 cellular and humoral immune responses. *J. Control. Release* **2013**, *165*, 16-21.
- 50
51
52 579 18. Gupta, A.; Stait-Gardner, T.; de Campo, L.; Waddington, L. J.; Kirby, N.; S. Price, W. S.;
53
54 580 Moghaddam, M. J. Nanoassemblies of Gd–DTPA–monooleyl and glycerol monooleate amphiphiles
55
56 581 as potential MRI contrast agents. *J. Mater. Chem. B* **2014**, *2*, 1225-1233.
- 57
58
59
60

- 1
2
3 582 19. Moghaddam, M. J.; de Campo, L.; Hirabayashi, M.; Bean, P. A.; Waddington, L. J.; Scoble,
4
5 583 J. A.; Coiac, G.; Drummond, C. J. Gadolinium-DTPA amphiphile nanoassemblies: agents for
6
7 584 magnetic resonance imaging and neutron capture therapy. *Biomater. Sci.* **2014**, *2*, 924-935.
- 8
9 585 20. Caltagirone, C.; Falchi, A. M.; Lampis, S.; Lippolis, V.; Meli, V.; Monduzzi, M.; Prodi, L.;
10
11 586 Schmidt, J.; Sgarzi, M.; Talmon, Y.; Bizzarri, R.; Murgia, S. Cancer Cell-Targeted Theranostic
12
13 587 Cubosomes. *Langmuir* **2014**, *30*, 6228-6236.
- 14
15
16 588 21. Deshpande, S.; Venugopal, E.; Ramagiri, S.; Bellare, J. R.; Kumaraswamy, G.; Singh, N.
17
18 589 Enhancing Cubosome Functionality by Coating with a Single Layer of Poly- ϵ -lysine. *ACS Appl.*
19
20 590 *Mater. Interfaces* **2014**, *6*, 17126-17133.
- 21
22
23 591 22. Muir, B. W.; Acharya, D. P.; Kennedy, D. F.; Mulet, X.; Evans, R. A.; Pereira, S. M.; Wark,
24
25 592 L. K.; Boyd, B. J.; Nguyen, T.-H.; Hinton, T. M.; Waddington, J. L.; Kirby, N.; Wright, D. K.;
26
27 593 Wang, H. X.; Egan, F. G.; Moffat, B. A. Metal-free and MRI visible theranostic lyotropic liquid
28
29 594 crystal nitroxide-based nanoparticles. *Biomaterials* **2012**, *33*, 2723.
- 30
31 595 23. Murgia, S.; Bonacchi, S.; Falchi, A. M.; Lampis, S.; Lippolis, V.; Meli, V.; Monduzzi, M.;
32
33 596 Prodi, L.; Schmidt, J.; Talmon, Y.; Caltagirone, C. Drug Loaded Fluorescent Cubosomes: Versatile
34
35 597 Nanoparticles for Potential Theranostic Applications. *Langmuir* **2013**, *29* (22), 6673-6679.
- 36
37
38 598 24. Murgia, S.; Falchi, A. M.; Meli, V.; Schillén, K.; Lippolis, V.; Monduzzi, M.; Rosa, A.;
39
40 599 Schmidt, J.; Talmon, Y.; Bizzarri, R.; Caltagirone, C. Cubosome formulations stabilized by a
41
42 600 dansyl-conjugated block copolymer for possible nanomedicine applications. *Colloids Surf. B* **2015**,
43
44 601 *129*, 87-94.
- 45
46
47 602 25. Nilsson, C.; Barrios-Lopez, B.; Kallinen, A.; Laurinmäki, P.; Butcher, S. J.; Raki, M.;
48
49 603 Weisell, J.; Bergström, K.; Larsen, S. W.; Østergaard, J.; Larsen, C.; Urtti, A.; Airaksinen, A. J.;
50
51 604 Yaghmur, A. SPECT/CT imaging of radiolabeled cubosomes and hexosomes for potential
52
53 605 theranostic applications. *Biomaterials* **2013**, *34*, 8491-8503.
- 54
55
56 606 26. Barreto, J. A.; O'Malley, W.; Kubeil, M.; Graham, B.; Stephan, H.; Spiccia, L.
57
58 607 Nanomaterials: applications in cancer imaging and therapy. *Adv. Mater.* **2011**, *23*, H18.

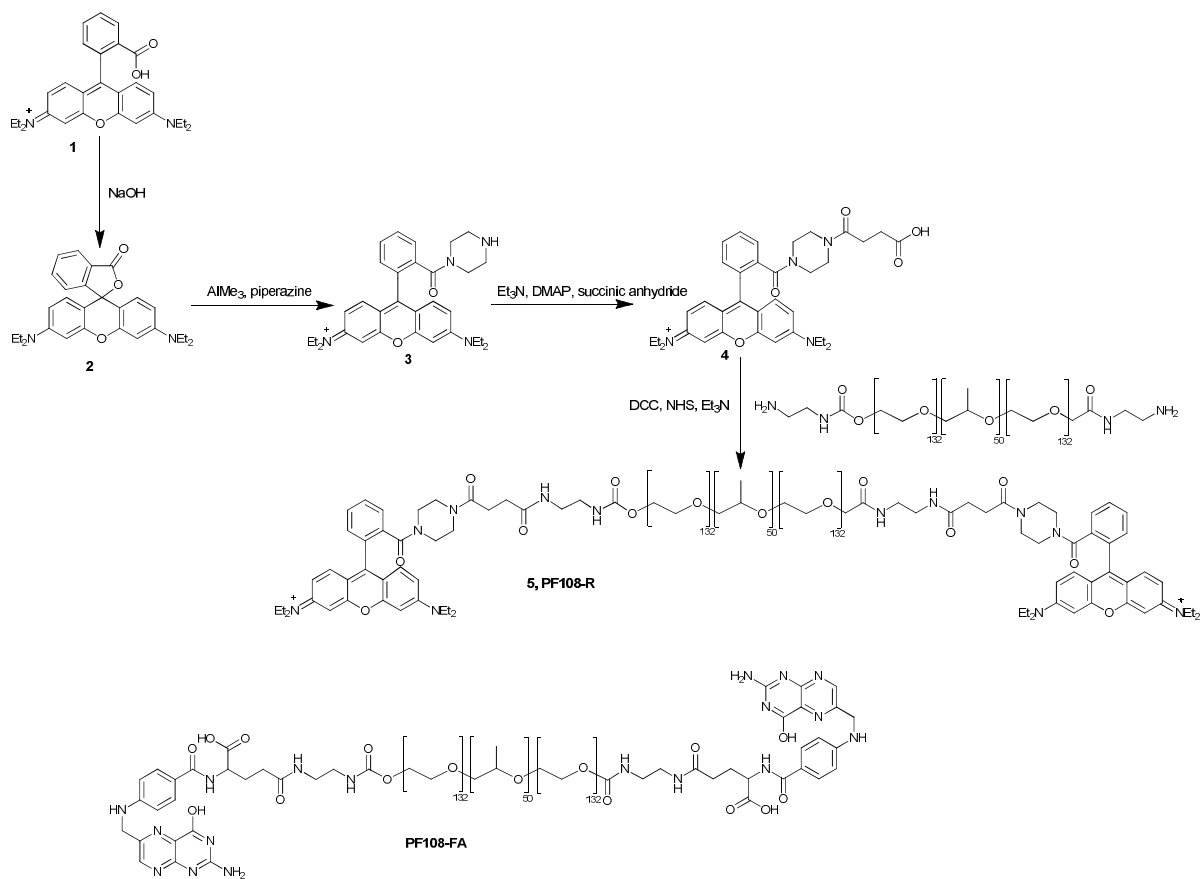
- 1
2
3 608 27. Pombo García, K.; Zarschler, K.; Barbaro, L.; Barreto, J. A.; O'Malley, W.; Spiccia, L.;
4
5 609 Stephan, H.; Graham, B. Zwitterionic-Coated "Stealth" Nanoparticles for Biomedical Applications:
6
7 610 Recent Advances in Countering Biomolecular Corona Formation and Uptake by the Mononuclear
8
9 611 Phagocyte System. *Small* **2014**, *10*, 2516–2529.
- 11 612 28. Caltagirone, C.; Arca, M.; Falchi, A. M.; Lippolis, V.; Meli, V.; Monduzzi, M.; Nylander,
12
13 613 T.; Rosa, A.; Schmidt, J.; Talmon, Y.; Murgia, S. Solvatochromic fluorescent BODIPY derivative
14
15 614 as imaging agent in camptothecin loaded hexosomes for possible theranostic applications. *RSC*
16
17 615 *Advances* **2015**, *5*, 23443–23449.
- 19 616 29. Zhai, J.; Scoble, J. A.; Li, N.; Lovrecz, G.; J. Waddington, L. J.; Tran, N.; Muir, B., W.;
20
21 617 Coia, G.; Kirby, N.; Drummond, C. J.; Mulet, X. Epidermal growth factor receptor-targeted lipid
22
23 618 nanoparticles retain self-assembled nanostructures and provide high specificity. *Nanoscale* **2015**, *7*,
24
25 619 2905-2913.
- 27 620 30. Falchi, A. M.; Rosa, A.; Atzeri, A.; Incani, A.; Lampis, S.; Meli, V.; Caltagirone, C.;
28
29 621 Murgia, S. Effects of monoolein-based cubosome formulations on lipid droplets and mitochondria
30
31 622 of HeLa cells. *Toxicol. Res.* **2015**, *4*, 1025-1036.
- 33 623 31. Janiak, J.; Bayati, S.; Galantini, L.; Pavel, N. V.; Schillén, K. Nanoparticles with a
34
35 624 Bicontinuous Cubic Internal Structure Formed by Cationic and Non-ionic Surfactants and an
36
37 625 Anionic Polyelectrolyte. *Langmuir* **2012**, *28*, 16536-16546.
- 39 626 32. Phillies, G. D. J. Experimental Demonstration of Multiple-Scattering Suppression in
40
41 627 Quasielastic-Light-Scattering Spectroscopy by Homodyne Coincidence Techniques. *Phys. Rev. A*
42
43 628 **1981**, *24*, 1939–1943.
- 45 629 33. Schätzel, K. Suppression of Multiple Scattering by Photon Cross-correlation Techniques. *J.*
46
47 630 *Mod. Opt.* **1991**, *38*, 1849–1865.
- 49 631 34. Urban, C.; Schurtenberger, P. Characterization of Turbid Colloidal Suspensions Using Light
50
51 632 Scattering Techniques Combined with Cross-Correlation Method. *J. Colloid Interface Sci.* **1998**,
52
53 633 *207*, 150–158.

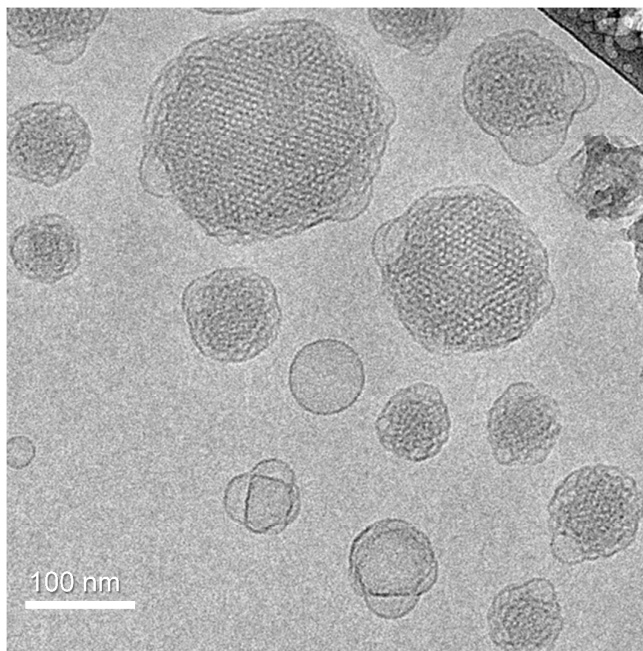
- 1
2
3 634 35. Block, I. D.; Scheffold, F. Modulated 3D cross-correlation light scattering: Improving turbid
4
5 635 sample characterization. *Rev. Sci. Instrum.* **2010**, *81*, 123107.
6
7 636 36. Liu, Z.; Liu, D.; Wang, L.; Zhang, J.; Zhang, N. Docetaxel-Loaded Pluronic P123 Polymeric
8
9 637 Micelles: in Vitro and in Vivo Evaluation. *Int. J. Mol. Sci.* **2011**, *12*, 1684-1696.
10
11 638 37. Caltagirone, C.; Bettoschi, A.; Garau, A.; Montis, R. Silica-based nanoparticles: a versatile
12
13 639 tool for the development of efficient imaging agents. *Chem. Soc. Rev.* **2015**, DOI:
14
15 640 10.1039/c4cs00270a.
16
17 641 38. Breul, A. M.; Hager, M. D.; Schubert, U. S. Fluorescent monomers as building blocks for
18
19 642 dye labeled polymers: synthesis and application in energy conversion, biolabeling and sensors.
20
21 643 *Chem. Soc. Rev.* **2013**, *42*, 5366--5407.
22
23 644 39. Nguyen, T.; Francis, M. B. Practical Synthetic Route to Functionalized Rhodamine Dyes.
24
25 645 *Org. Lett.* **2003**, *5*, 3245-3248.
26
27 646 40. Zhang, W.; Shi, Y.; Chen, Y.; Ye, J.; Sha, X.; Fang, X. Multifunctional Pluronic P123/F127
28
29 647 mixed polymeric micelles loaded with paclitaxel for the treatment of multidrug resistant tumors.
30
31 648 *Biomaterials* **2011**, *32*, 2894-2906.
32
33 649 41. Murgia, S.; Falchi, A. M.; Mano, M.; Lampis, S.; Angius, R.; Carnerup, A. M.; Schmidt, J.;
34
35 650 Diaz, G.; Giacca, M.; Talmon, Y.; Monduzzi, M. Nanoparticles from lipid-based liquid crystals:
36
37 651 emulsifier influence on morphology and cytotoxicity. *J. Phys. Chem. B* **2010**, *114* (10), 3518-3525.
38
39 652 42. Barauskas, J.; Markus Johnsson, M.; Joabsson, F.; Tiberg, F. Cubic Phase Nanoparticles
40
41 653 (Cubosome[†]): Principles for Controlling Size, Structure, and Stability. *Langmuir* **2005**, *21*, 2569-
42
43 654 2577.
44
45 655 43. Nakano, M.; Sugita, A.; Matsuoka, H.; Handa, T. Small-Angle X-ray Scattering and ¹³C
46
47 656 NMR Investigation on the Internal Structure of "Cubosomes". *Langmuir* **2001**, *17*, 3917-3922.
48
49 657 44. Beija, M.; Afonso, C. A. M.; Martinho, J. M. G. Synthesis and applications of Rhodamine
50
51 658 derivatives as fluorescent probes. *Chem. Soc. Rev.* **2009**, *38*, 2410-2433.
52
53
54
55
56
57
58
59
60

- 1
2
3 659 45. Lavis, L. D.; Chao, T.-Y.; Raines, R. T. Fluorogenic Label for Biomolecular Imaging. *ACS*
4
5 660 *Chem. Biol.* **2006**, *1*, 252-260.
- 6
7 661 46. Domingo-Domenech, J.; Oliva, C.; Rovira, A.; Codony-Servat, J.; Bosch, M.; Filella, X.;
8
9 662 Montagut, C.; Tapia, M.; Campás, C.; Dang, L.; Rolfe, M.; Ross, J. S.; Gascon, P.; Albanell, J.;
10
11 663 Mellado, B. Interleukin 6, a nuclear factor-kappaB target, predicts resistance to docetaxel in
12
13 664 hormone-independent prostate cancer and nuclear factor-kappaB inhibition by PS-1145 enhances
14
15 665 docetaxel antitumor activity. *Clin. Cancer Res.* **2006**, *12*, 5578-86.
- 16
17
18 666 47. Zhu, S.; Oremo, J. A.; Li, S.; Zhen, M.; Tang, Y.; Du, Y. Synergistic antitumor activities of
19
20 667 docetaxel and octreotide associated with apoptotic-upregulation in castration-resistant prostate
21
22 668 cancer. *PLoS One* **2014**, *9*, e91817.
- 23
24
25 669 48. Zhu, H.; Chen, H.; Zeng, X.; Wang, Z.; Zhang, X.; Wu, Y.; Gao, Y.; Zhang, J.; Liu, K.; Liu,
26
27 670 R.; Cai, L.; Mei, L.; Feng, S. S. Co-delivery of chemotherapeutic drugs with vitamin E TPGS by
28
29 671 porous PLGA nanoparticles for enhanced chemotherapy against multi-drug resistance. *Biomaterials*
30
31 672 **2014**, *35*, 2391-2400.
- 32
33
34 673 49. Shen, H.; Lee, F. Y.; Gan, J. Ixabepilone, a novel microtubule-targeting agent for breast
35
36 674 cancer, is a substrate for P-glycoprotein (P-gp/MDR1/ABCB1) but not breast cancer resistance
37
38 675 protein (BCRP/ABCG2). *J. Pharmacol. Exp. Ther.* **2011**, *337*, 423-432.
- 39
40
41 676 50. Chung, H.; Caffrey, M. The Neutral Area Surface of the Cubic Mesophase:
42
43 677 Location and Properties. *Biophys. J.* **1994**, *66*, 377-381.
- 44
45 678 51. Hyde, S. Bicontinuous structures in lyotropic liquid crystals and crystalline hyperbolic
46
47 679 surfaces. *Curr. Opin. Solid State Mater. Sci.* **1996**, *1*, 653-662.

680

681





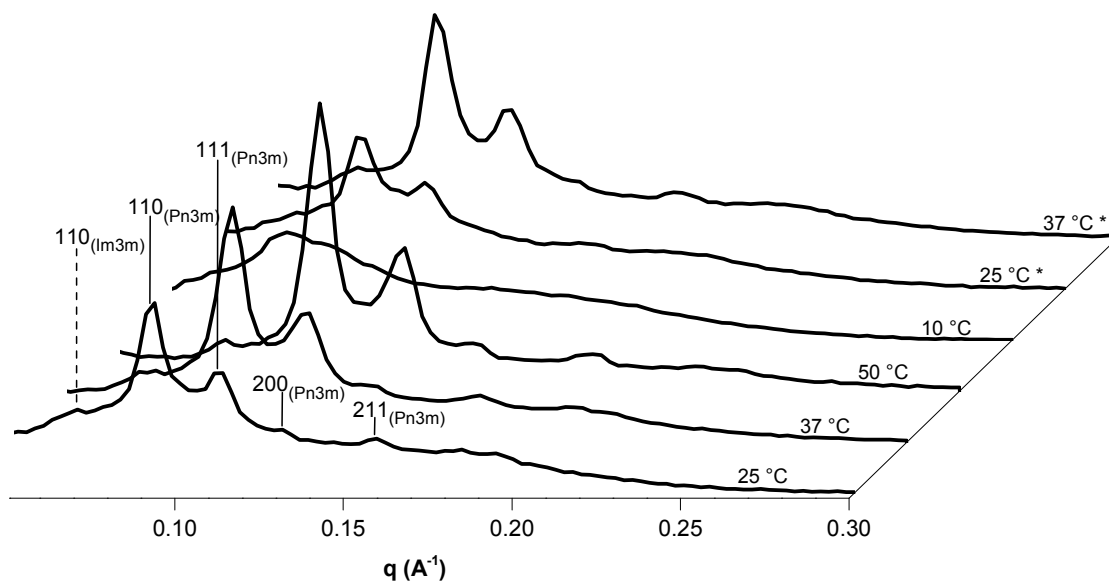
687

688

689 **Figure 1.** Cryo-TEM image of the cubosome formulation stabilized by a 60/20/20 mixture of

690 commercial PF108, folate-conjugated PF108, and rhodamine-conjugated PF108.

691



692

693

694 **Figure 2.** $I(q)$ vs q data obtained by SAXS recorded at different temperatures of the cubosome
695 formulation stabilized by the same Pluronic mixture as in Figure 1. The Miller indices are reported
696 on top of the corresponding Bragg peaks with the indication of the space group in the case of the
697 bicontinuous cubic phases.

698

699

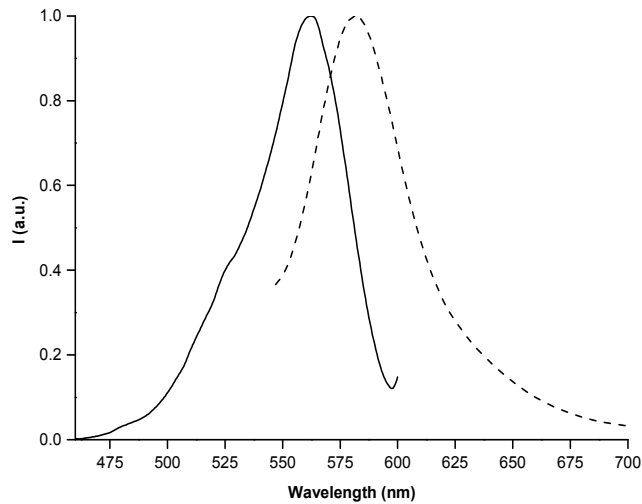
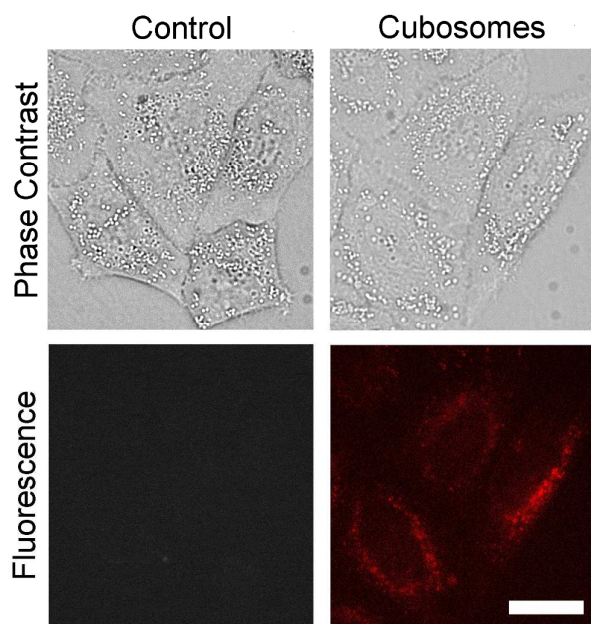


Figure 3. Normalized emission ($\lambda_{\text{exc}} = 522$ nm) and excitation ($\lambda_{\text{em}} = 581$ nm) spectra of the aqueous cubosome formulation stabilized using the same Pluronic mixture as in Figure 1.

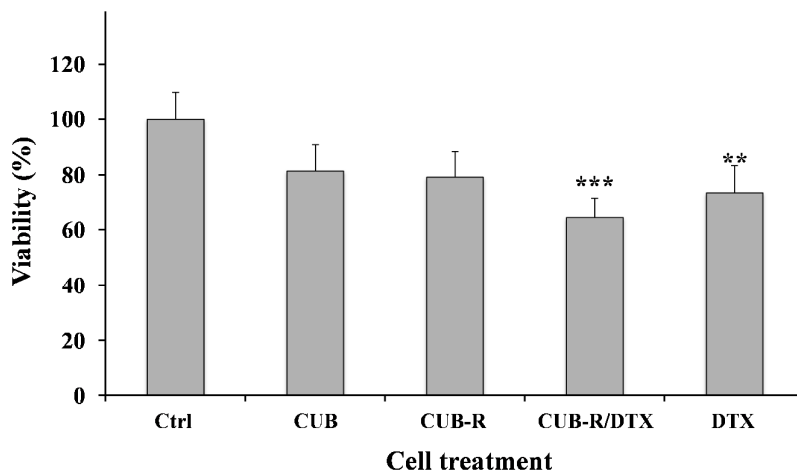


709 **Figure 4.** Fluorescence microscopy of living HeLa cells treated with cubosomes not carrying the
710 drug (incubation for 4 h) showing a diffuse cytoplasmic fluorescence in treated cells indicating
711 nanoparticle uptake. Scale bar = 20 μm .

712

713

714



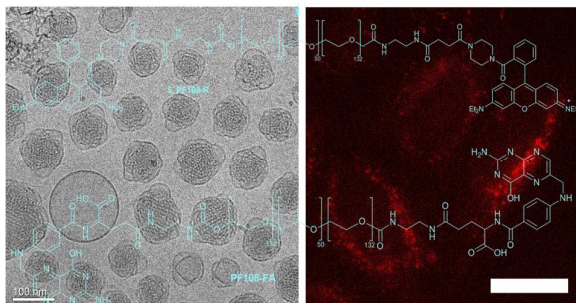
715

716

717 **Figure 5.** Viability, expressed as % of the control, induced in HeLa cells by incubation for 4 h in
718 the presence of different type of cubosome formulations (CUB, CUB-R, and CUB-R/DTX, see the
719 text) and Docetaxel (DTX). Drug concentration in the CUB-R/DTX formulation (0.8 μM) is 12.5-
720 fold lower than in DTX molecular dispersion (10 μM). Results are expressed as a mean \pm standard
721 deviation (SD) of four independent experiments involving quadruplicate analyses for each sample
722 ($n = 4$). *** = $P < 0.001$; ** = $P < 0.01$ versus Ctrl, and data were analyzed using one-way
723 ANOVA.

724

1
2
3 725 TOC
4 726
5 727



728
729